Chemical Engineering Journal 504 (2025) 158726

Contents lists available at ScienceDirect

Chemical Engineering Journal

journal homepage: www.elsevier.com/locate/cej

Development of ceria-supported metal-oxide (MO_x/CeO_2) catalysts via a one-pot chemical vapor deposition (OP-CVD) technique: Structure and reverse water gas shift reaction study

Amol Pophali [a,1], Ryuichi Shimogawa [a,b,1], Lihua Zhang [c], Gihan Kwon [d], Kwangsuk Yoon [e], Jangeon Roh [f], Do Heui Kim [f], Hocheol Song [e], Anatoly I. Frenkel [a,g], Taejin Kim [a,*]

[a] Department of Materials Science and Chemical Engineering, Stony Brook University, Stony Brook, NY, 11794, USA
[b] Mitsubishi Chemical Corporation, Science & Innovation Center, 1000, Kamoshida-cho, Aoba-ku, Yokohama 227-8502, Japan
[c] Center for Functional Nanomaterials, Brookhaven National Laboratory, Upton, NY 11973, USA
[d] National Synchrotron Light Source II, Brookhaven National Laboratory, Upton, NY 11973, USA
[e] Department of Resource and Environmental Engineering, Hanyang University, Seoul, 04763, Republic of Korea
[f] School of Chemical and Biological Engineering, Institute of Chemical Processes, Seoul National University, 1 Gwanak-ro, Gwanak-Gu, Seoul 08826, Republic of Korea
[g] Chemistry Division, Brookhaven National Laboratory, Upton, NY 11973, USA

ARTICLE INFO

Keywords:
Catalysts
One-pot chemical vapor deposition
Organometallic precursor
Monomer
Reverse water gas shift reaction
Ceria

ABSTRACT

Current synthesis techniques for metal oxide (MO_x)-supported catalysts have certain limitations of undesired target loading, ineffective dispersion of active species over the surface, uncontrolled particle size of active species, and complicated synthesis steps. We developed a one-pot chemical vapor deposition (OP-CVD) methodology; by using which a solid metal precursor forms a vapor in a controlled condition and gets supported over the surrounding matrix. The theoretical stability followed by experimental validation using TGA is crucial for selecting the metal precursors. Three simple steps viz. premixing, dispersion, and rapid fixation by calcination are involved in the catalyst development via the OP-CVD approach. This study solely focused on the synthesis of 3d transition MO_x over ceria support. The physicochemical characterizations of the prepared catalysts were performed by XRD, ICP-OES, SEM-EDX, CO pulse chemisorption, XANES, and EXAFS analyses to understand the crystal structure of involved species, target metal loading, dispersion, and particle size and prove the feasibility and viability of OP-CVD. The prepared catalysts were further tested for reverse water gas shift (RWGS) reaction to link their structural information with activity. The RWGS reaction data showed that the CO activity and CO selectivity were metal - and metal precursor-dependent. Higher CO activity of > 0.1 mol/h g-cat was observed for Cu and Co-based catalysts, with CO selectivity of ~100 %. This study provides an opportunity to produce efficient supported catalysts in a convenient way, providing effective catalytic activity.

1. Introduction

1.1. Background

Catalysts play a crucial role in chemical reactions involving liquid and gas phase industrial processes. The active component of many catalysts typically employs nanoparticles (NPs) of metals (M) or metal oxides (MO_x) from the platinum group (Pt, Pd, Rh, Ru, etc.) [1,2] as well as the non-platinum group transition (Ni, Co, Cu, Fe, etc.) [3,4] metals. These M and MO_x NPs are located throughout a thermally stable support material such as ceria (CeO_2), alumina (Al_2O_3), silica (SiO_2), titania (TiO_2), or activated carbon (C) [5]. A primary challenge in catalyst synthesis is the achievement of a narrow particle size distribution and high dispersion of M/MO_x on the support, essential for maximizing activity and selectivity [6]. The synthesis of catalysts with small sizes and the prevention of the intrinsic propensity of aggregation are among the important challenges for catalyst preparation. The synthesis method significantly impacts the catalyst's performance, influencing its activity,

* Corresponding author.
E-mail addresses: amol.pophali@stonybrook.edu (A. Pophali), ryuichi.shimogawa@stonybrook.edu (R. Shimogawa), taejin.kim@stonybrook.edu (T. Kim).
[1] These authors contributed equally.

https://doi.org/10.1016/j.cej.2024.158726
Received 20 August 2024; Received in revised form 16 November 2024; Accepted 17 December 2024
Available online 17 December 2024

selectivity, and stability, thereby affecting its effectiveness in industrial processes.

Historically, several methodologies have been employed for catalyst synthesis, with impregnation (including wet, dry, or incipient wetness impregnation (IWI)) being the most prevalent [7]. In these methods, the metal-associated medium deposits into the pores of the support surface by the capillary pressure gradient. The precipitation method, which includes coprecipitation and deposition precipitation, involves selecting suitable metal salts and bases to produce precipitates that form the catalyst [8]. The catalysts prepared by impregnation and precipitation processes have larger-sized active sites and poor surface dispersion [9]. Additionally, melt infiltration has been utilized to create supported catalysts. However, this process can result in non-uniform distribution and agglomeration during the precursor's decomposition phase due to the mobility of the precursor on the surface [10]. Alternative techniques such as the colloidal method, microemulsion, and reverse microemulsion have also been explored, allowing controlled synthesis but facing complexities and scalability challenges at a commercial level [10]. Atomic layer deposition (ALD) provides a remedy up to a certain extent but is limited by expensive and complex instrumentation [11]. Therefore, a simple, effective, and economically viable synthesis method needs to be developed for the synthesis of efficient supported M (or MO_x) catalysts.

Most supported catalysts exist in the form of small-sized active phases in the high-surface-area and thermally stable support matrix. Usually, a metal oxide support, such as silica (SiO_2), alumina (Al_2O_3), ceria (CeO_2), or titania (TiO_2), is used for gas phase reactions. The choice of support material is based on the requirement of metal-support interactions (MSI) for the reaction. It is speculated that MSI plays a crucial role in the improvement of the reactivity and catalyst durability. Particularly, ceria is reported to show involvement in MSI due to its redox ability to cycle from Ce^{+3} to Ce^{+4}, and vice versa. Also, oxygen storage capacity and spillover at the active site-ceria interface are important factors as well. In addition, ceria can provide high surface area and thermal stability under harsh conditions. Thus, ceria has been extensively used as a promising support and has applications in emission control, automotive, water–gas shift, reforming, oxidation, and electrochemical reactions [12–14].

1.2. Hypothesis

To overcome the drawbacks of the existing catalyst synthesis methodologies and the development of quality-supported catalysts, the authors developed a one-pot-chemical vapor deposition (OP-CVD) method. Our hypothesis behind this method is that the conventional liquid phase synthetic method is dominated by the thermodynamics that can be explained by the classical nucleation theory, where the critical radius determines the minimum particle size, and we need to develop a method that can be kinetically controlled in order to overcome this limit [15]. OP-CVD method consists of three key components: (1) Design of the organometallic precursor, (2) Gas phase deposition for kinetic control of the process, and (3) Rapid fixation process (decomposition of organometallic precursor).

For the design of the organometallic precursor, we have established the following criteria: (i) Stable monomeric structure: The precursor should be in a solid phase, have a low molecular weight, and be coordinatively saturated as a monomer to ensure structural stability. If it is unsaturated, it must be sterically hindered to prevent the oligomerization of the complex. (ii) Vapor pressure: The precursor should exhibit sufficient vapor pressure to facilitate its use in vapor deposition processes. (iii) Ligand composition: The ligand must be composed of elements (preferably carbon, hydrogen, or oxygen) that can be effectively removed by oxidation or reduction, simplifying the purification process. (iv) Thermal stability: Under inert gas conditions, thermogravimetric analysis (TGA) should show that the precursor vaporizes before any decomposition occurs, ensuring high thermal stability and clean evaporation.

The deposition process is a thermal treatment to facilitate gas-phase deposition, which achieves kinetic control of the process. The main driving force behind the dispersion of the solid precursors is their physical adsorption to the high surface area of the support, which will be designed based on TGA analysis. Subsequently, the rapid fixation process is initiated by changing the atmospheric conditions to either oxidative or reductive states, followed by thermal treatment. This promotes the decomposition of the organometallic precursor while preventing further vaporization from the support, thereby reversing the order of the vaporization step versus the decomposition step. This step is crucial in ensuring that the metals are fixed to the positions that were located by the gas-phase deposition. This integrated approach not only enhances the control and efficiency of catalyst synthesis but also differentiates OP-CVD from similar methods like Metal Organic Chemical Vapor Deposition (MOCVD) [16,17], which conducts gas-phase deposition and decomposition under similar thermal conditions but does not specify explicit conditions for the fixation process. The design of suitable precursors tailored for OP-CVD further enhances the method's specificity and effectiveness.

In this study, we report on the OP-CVD method for the synthesis of MO_x (or M) supported catalysts and demonstrate it by synthesizing a series of MO_x/CeO_2 catalysts using Cr, Mn, Fe, Co, Ni, and Cu metal-based organometallic precursors. We also discuss the effect of the precursor design leading to the significant change in the dispersion of surface species, metal loading, and the activity and selectivity of the reverse water gas shift reaction (RWGS), which we choose as a model reaction. The overall results let us conclude: (i) the feasibility of the OP-CVD method for synthesis of supported catalysts overcoming the drawbacks of existing methods; (ii) characterization results reveal the effectiveness of the precursor design, deposition, and rapid fixation steps in OP-CVD; (iii) catalysts developed by OP-CVD protocol reveal high activity towards RWGS reaction with desired selectivity.

2. Materials and methods

2.1. Chemicals

The ceria (HSA5) support used in this study was provided by Rhodia. All the metal precursors were purchased from Sigma Aldrich, USA, including nickel(II) bis(2,2,6,6-tetramethyl-3,5-heptanedionate) (Ni $(tmhd)_2$, 99%), nickel(II) acetylacetonate (Ni$(acac)_2$, 99%), cobalt(III) acetylacetonate (Co$(acac)_3$, 99%), cobalt(II) acetylacetonate (Co$(acac)_2$, 99%), copper(II) acetylacetonate (Cu$(acac)_2$, 99%), chromium(III) acetylacetonate (Cr$(acac)_3$, 99%), Manganese(III) tris(2,2,6,6tetramethyl-3,5-heptanedionate) (Mn$(tmhd)_3$, 99%) and ferrocene (bis(η^5-cyclopentadienyl)iron, 99%). The gases used in this study for synthesis viz. nitrogen (N_2, UHP grade), dry air (20% O_2, 80% N_2), and hydrogen (5% H_2 balanced with N_2) were purchased from Airgas Inc., USA. Nitric acid (70%) for analysis was purchased from Sigma Aldrich, Germany. The gases used for the RWGS reaction were carbon dioxide (CO_2, UHP grade) and hydrogen (5% H_2 balanced with He) and purchased from Airgas Inc., USA.

2.2. Synthesis

The schematics for the synthesis using OP-CVD are presented in Fig. 1. Ceria (1 g) and metal precursor (0.031 g-metal) were thoroughly mixed (15 min) in a mortar-pestle, without any addition of liquid solvents, to get a uniform physical mixture of the associated powders (Fig. 1a). This mixture was evenly distributed throughout a combustion boat (Coors^{TM} high alumina combustion boat) and the boat was placed in a horizontal quartz tubular reactor (23.8 mm OD). The reactor was then placed over a horizontal tubular furnace (Lindberg/Blue Mini-Mite, Thermo Scientific). The mixture was heated at the furnace temperature specified in Table 1 (heating rate 10 °C/min), under N_2 flow at 20 ml/

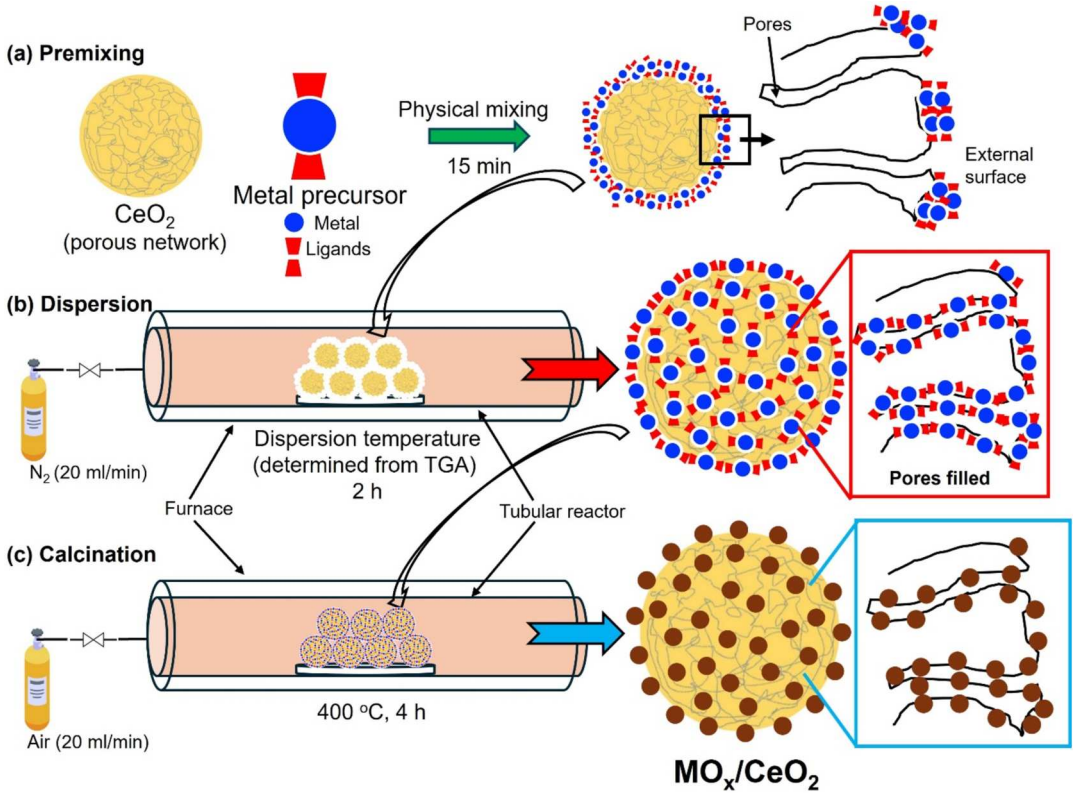

Fig. 1. Schematics for synthesis procedure of MO_x/CeO_2 by OP-CVD method.

Table 1
Synthesis details and ICP-OES data of 3 wt% MO_x/CeO_2 prepared using OP-CVD.

Entry	Metal	Precursor	Dispersion temperature (°C)	Actual metal loading (wt%)
1	Co	$Co(acac)_3$	165	2.94
2	Co	$Co(acac)_2$	135	2.96
3	Ni	$Ni(tmhd)_2$	135	2.98
4	Ni	$Ni(acac)_2$	155	3.00
5	Cr	$Cr(acac)_3$	160	2.98
6	Mn	$Mn(tmhd)_3$	135	2.79
7	Fe	Ferrocene	65	2.96
8	Cu	$Cu(acac)_2$	155	2.80

min (Fig. 1b). Then, dry air (20% O_2, 80% N_2) flowed at 20 ml/min, and the mixture was heated at 400 °C (heating rate 10 °C/min) for 4h (Fig. 1c). After cooling to the ambient temperature, the prepared MO_x/CeO_2 catalyst was sieved (500 μm, Fieldmaster) and stored into a vial.

2.3. Catalyst characterization

Several physicochemical characterization techniques were used to understand the catalyst properties and configuration.

2.3.1. Thermogravimetric analysis (TGA)

The metal precursors were tested for weight loss due to thermal effects using thermogravimetric analysis (TGA) (Q500, TA instruments USA). Tests were carried out in two separate procedures (e.g., normal and programmed): (1) normal TGA from room temperature (RT) to 900 °C at 10 °C/min under N_2 flowing; and (2) programmed TGA in temperature range corresponding to ~99.9 to ~95% weight under N_2 flowing. The programmed TGA analysis was performed at a step of every 10 °C in the defined range with 1h holding time. These thermal analysis data were performed to determine the suitable temperature conditions for catalyst synthesis.

2.3.2. X-ray diffraction (XRD)

The samples were tested for high-energy X-ray diffraction (XRD) at 28-ID-1 PDF beamline ($\lambda = 0.1665$ Å) at the National Synchrotron Light Source II (NSLS-II), Brookhaven National Laboratory, USA. The catalyst samples were filled in polyimide (1 mm OD) tubes. The extraction of the XRD data and further analysis were done by the Dioptas software.

2.3.3. Scanning electron microscopy (SEM)

The Scanning electron microscopy (SEM) (JEOL JSM-7600F) tests were performed to understand the morphology of the synthesized materials. Energy-dispersive X-ray spectroscopy (Oxford Instruments, UK) mapping analysis was performed on the MO_x/CeO_2-based catalyst to observe the elemental distributions throughout the catalyst material.

2.3.4. X-ray absorption spectroscopy (XAS)

X-ray absorption spectroscopy (XAS) measurements were performed at the QAS Beamline (7-BM) of National Synchrotron Light Source II (NSLS II), Brookhaven National Laboratory. The fluorescence signals were collected using the Canberra PIPS detector for the Co K edge and the PerkinElmer 1621 area detector for the Ni K edge equipped at the beamline. Co K edge spectra were collected in fluorescence mode with a 3μm Fe filter for CoO_x/CeO_2 samples. The CoO_x/CeO_2 and NiO_x/CeO_2 pellets were prepared by pressurizing a CoO_x/CeO_2 and NiO_x/CeO_2 powder in a 13 mm die using a hydraulic press. The fluorescence detector was located at 90° respective to the incident beam. Data processing and analysis were performed with Athena, Artemis, and FEFF6.2 programs from the Demeter package [18]. The nearest neighboring Co-O (1st shell), Co(octahedral site)–Co(octahedral site) (2nd shell), and Co (octahedral site)–Co(tetrahedral site) or Co(tetrahedral site)–Co(octahedral site) (3rd shell) theoretical photoelectron paths calculated with FEFF for the Co_3O_4 structure were used to fit the experimental data for the CoO_x/CeO_2 catalysts [19]. The contributions of the paths corresponding to the Co(tetrahedral site)–Co(tetrahedral site) were low compared to the paths corresponding to the 3rd shell described above

and were excluded from the model. The fitting parameters were the corrections to the model distances, the coordination number, the Debye-Waller factor (the mean square disorder of the distances), and the correction to the energy origin. The amplitude reduction factor (S_0^2 = 0.79) was found from the fit to the Co_3O_4 reference sample and fixed in the analysis of CoO_x/CeO_2 data. For extracting the information about the fractions of CoO and Co_3O_4 phases in CoO_x/CeO_2, linear combination fitting (LCF) was applied to the XANES region of the XAS measurement. The LCF was carried out in normalized absorption with Co_3O_4 and CoO standards in an energy range of −20 to 60 eV with respect to the edge energy of the sample (7720.8 eV). The relative weights of the components were allowed to vary from 0 to 1. For NiO_x/CeO_2, Ni K edge spectra were collected in fluorescence mode for the NiO_x/CeO_2 samples using the region of interest set at $K\alpha_1$ and $K\alpha_2$ fluorescence lines. The nearest neighboring Ni-O (1st shell) and Ni-Ni (2nd shell) theoretical photoelectron paths calculated with FEFF for the NiO structure were used to fit the experimental data for the NiO_x/CeO_2 catalysts. The fitting parameters included the corrections to the model distances, the coordination number, the Debye-Waller factor, and the correction to the energy origin. The amplitude reduction factor ($S_0^2 = 1.0$) was determined from the fit to the NiO reference sample and fixed during the analysis of the NiO_x/CeO_2 data.

2.3.5. Inductively coupled plasma optical emission spectroscopy (ICP-OES)

The metal or surface species content in the series of MO_x/CeO_2 catalysts was determined using inductively coupled plasma optical emission spectroscopy (ICP-OES). This technique was performed on Optima 5300 DV (PerkinElmer, USA) spectrometer. The samples were dissolved in nitric acid and digested in a microwave digestion system (ETHOS TC, Milestone, Italy) before testing. As a reference, an ICP multi-element standard solution XVI (Merck, Germany) was used.

2.3.6. CO pulse chemisorption

Pulse CO chemisorption measurements were performed to analyze the catalysts' exposed MO_x sites. Chemisorption tests were performed using BEL-CAT-II (MicrotracBEL., Corp.) coupled with TCD at 50 °C. The samples: NiO_x/CeO_2 ($Ni(tmhd)_2$), NiO_x/CeO_2 ($Ni(acac)_2$), CoO_x/CeO_2 ($Co(acac)_3$), and CoO_x/CeO_2 ($Co(acac)_2$) were investigated for the associated metal dispersion. The NiO_x/CeO_2 and CoO_x/CeO_2 samples underwent reduction pretreatment at 500 °C and 400 °C for 30 min, respectively, under 5% H_2/Ar (50 ml/min) conditions. CO pulses were utilized until the samples reached saturation when the temperature was lowered to −78 °C. For consistency of the measurement, 7 CO pulses were provided to reach adsorption saturation in each sample. The dispersion of metal, D (%), was computed from the following equation:

$$\text{Metal dispersion, D (\%)} = \left(\frac{V \times SF \times MW}{V_{mol} \times c/100}\right) \times 100 \quad (1)$$

where V is the volume of adsorbed CO per catalyst weight; SF is the stoichiometric factor (SF = 2 for Ni and Co); MW is the molar mass of metal (Ni: 58.69 and Co: 58.93 g/mol); V_{mol} is the standard molar volume of CO (22414 cm^3/mol), and c is the actual metal loading in the catalyst (wt%). The average particle diameter calculations were also performed using the following equations:

$$\text{Metal surface area, } A_m\ (m^2/g) = \frac{V \times 6.02 \times 10^{23} \times SF \times \sigma_m \times 10^{-18}}{V_{mol}} \quad (2)$$

$$\text{Average particle diameter (nm)} = \frac{60 \times c}{A_m \times \rho} \quad (3)$$

where σ_m and ρ is the cross-sectional area and density of the supported metal, respectively. The average particle diameter calculations were performed with assumption of σ_m for Ni (0.065 nm^2) and Co (0.066 nm^2). The ρ value for both metals were 8.9 g/cm^3.

2.4. RWGS reaction tests

Quartz tube (Inner diameter: 2.00 mm) was charged with quartz wool and the catalyst (15 mg) and set to the Clausen cell [20]. The mixed gas of 4.8%CO_2, 4.8%H_2, and 90.5%He were flowed in a total of 42 sccm, and the reaction temperature was increased incrementally from ambient temperature to 500 °C. The outlet gas (CO_2, CO, and CH_4) were measured using a gas chromatograph (Agilent 7890B, column: HP-PLOT Molesieve GC Column, 30 m×0.53 mm, 25.00 μm and HP-PLOT Q GC Column, 30 m×0.53 mm, 40.00 μm, isothermal measurement at 60°C, carrier gas: He). A thermal conductivity detector (TCD) was used to quantify CO_2 and CO, and a flame ionization detector (FID) was used to quantify CH_4. The outlet gas was also monitored by the mass spectrometer (Hiden QGA) to confirm there were no other side products. Conversion, activity, and selectivity were calculated according to the following equations:

$$\text{Conversion (\%)} = \left(1 - \frac{[CO_2]}{[CO_2] + [CO] + [CH_4]}\right) \times 100 \quad (4)$$

$$WHSV\left(\frac{L}{h \cdot g_{cat}}\right) = F_{total} \times \frac{60}{1000} \times \frac{1}{w_{cat}} \quad (5)$$

$$\text{Activity}\left(\frac{mol}{h \cdot g_{cat}}\right) = WHSV \times ([CO] + [CH_4]) \times \frac{RT}{P} \quad (6)$$

$$\text{CO Selectivity (\%)} = \frac{[CO]}{[CO] + [CH_4]} \times 100 \quad (7)$$

$$\text{CH_4 Selectivity (\%)} = \frac{[CH_4]}{[CO] + [CH_4]} \times 100 \quad (8)$$

F_{total}(sccm) is the total gas flow of the input, w_{cat} is the weight of the catalyst (g), R is the gas constant, T is the absolute temperature, and P is the ambient pressure. The CO and CH_4 selectivity (equation (7) and (8)) were calculated as per the carbon balance in the product stream only.

3. Results

3.1. Thermal stability of metal precursors

To study the thermal behavior of precursors in an inert condition, the metal precursors were tested for TGA (Fig. 2 and Fig. S1) prior to their application for OP-CVD. These tests discern whether a precursor will predominantly undergo (1) vaporization, leaving virtually no residue, or (2) decomposition, leaving behind a residue of the non-volatile metal. As shown in Fig. 2a and 2d, the $Ni(acac)_2$ and $Co(acac)_2$, there was a significant amount of residual weight (dotted line) observed even up to 900 °C: ~20% for $Ni(acac)_2$ and ~14% for $Co(acac)_2$. This is clear evidence that the precursors decomposed by dissociation of the ligands rather than the vaporization of the whole complex. The metal content in $Ni(acac)_2$ is ~22.8 (wt%), and it is agreed that most of the precursors favor decomposition over vaporization. The metal content of $Co(acac)_2$ precursor is ~22.9 (wt%), showing the possibility of a competitive process of decomposition and vaporization present. Conversely, as demonstrated in Fig. 2b and Fig. 2e for $Ni(tmhd)_2$ and $Co(acac)_3$, respectively, the residual weights were negligible (~0 wt%), indicating a preference for vaporization over decomposition.

This difference in the thermal behavior of precursors can be attributed to the stability of their monomeric structures. The vapor pressure is known to have a strong correlation with the molecular weight, and therefore, the monomeric structure is far more volatile than the oligomeric structure. The crystal structures of $Ni(acac)_2$ and $Co(acac)_2$ are known to be trimeric and tetrameric, respectively [21,22]. In contrast, the crystal structures of $Ni(tmhd)_2$ and $Co(acac)_3$ are monomeric [23,24]. $Ni(acac)_2$ is a $16e^-$ complex as a monomer, which is

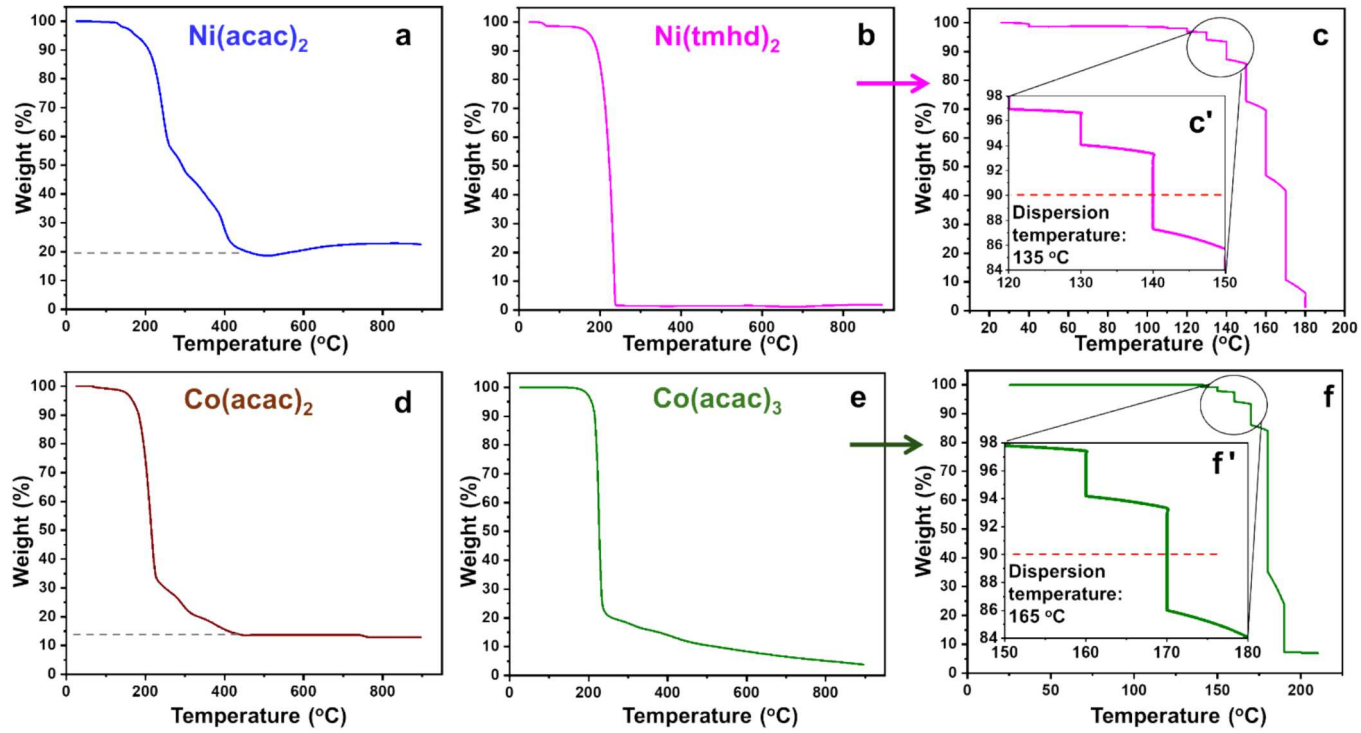

Fig. 2. TGA plots of Ni precursors: (a) $Ni(acac)_2$, (b) $Ni(tmhd)_2$, (c-c') programmed TGA for $Ni(tmhd)_2$; and Co precursors: (d) $Co(acac)_2$, (e) $Co(acac)_3$, (f-f') programmed TGA for $Co(acac)_3$.

coordinatively unsaturated and favors the oligomeric structure to fulfill the effective atomic number (EAN) rule. The introduction of the sterically hindered ligand stabilizes the monomeric structure by the steric repulsion of the "tBu" groups. $Co(acac)_2$ is a 15e$^-$ complex as a monomer, and it is coordinatively unsaturated, while $Co(acac)_3$ is an 18e$^-$ complex as a monomer, and it fulfills the EAN rules.

Fig. 2c and 2f present the programmed TGA plots for $Ni(tmhd)_2$ and $Co(acac)_3$, respectively. The temperature corresponding to 10% weight loss was designated as the dispersion temperature. According to the programmed TGA results, the dispersion temperatures for $Ni(tmhd)_2$ and $Co(acac)_3$ are 135°C and 155°C, respectively. The rationale behind selecting the dispersion temperature was to identify a temperature sufficiently high to enable the precursor to volatilize and disperse effectively through the catalyst support (ceria in this work), yet low enough to prevent the loss of the precursors from the system entirely. We note that the weight loss observed during the synthesis is expected to be significantly lower than in the actual synthetic process due to the adsorption of precursors by the high-surface-area support.

The normal and programmed TGA results for other precursors (e.g., ferrocene, $Cu(acac)_2$, $Cr(acac)_3$, and $Mn(tmhd)_3$) is presented in Fig. S1. Based on the TGA results, it is concluded that the precursors contain monomeric structure since complete weight loss of the precursors was achieved. The dispersion temperatures for the precursors were also determined by the programmed TGA results (Fig. S1(a', b', c', and d')): Ferrocene (65 °C), $Cu(acac)_2$ (155 °C), $Cr(acac)_3$ (160 °C), and $Mn(tmhd)_3$ (135 °C).

3.2. XRD analysis

The XRD technique was utilized to investigate the influence of different precursors on the crystalline structures of the synthesized catalysts. The XRD patterns of the NiO_x/CeO_2 and CoO_x/CeO_2 catalysts that were synthesized from two different precursors are shown in Fig. 3. For comparison purposes, the XRD pattern for bulk CeO_2 was also included. The XRD patterns of all NiO_x/CeO_2 and CoO_x/CeO_2 catalysts exhibited peaks corresponding to diffraction peaks of CeO_2: the peaks at

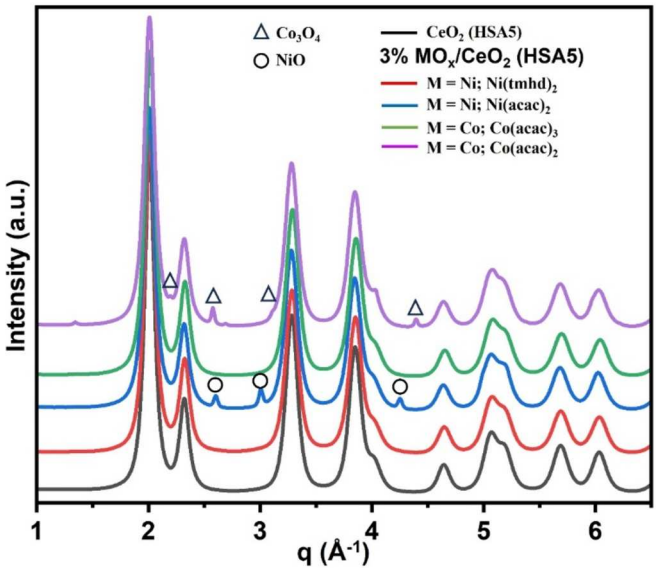

Fig. 3. XRD plots for ceria-supported NiO_x and CoO_x catalysts with different precursors.

q values 2.0, 2.3, 3.3, 3.85, 4.0, 4.64, 5.0, 5.2, 5.7, and 6.03 Å^{-1} correspond to the (111), (200), (220), (311), (222), (400), (331), (420), (422), and (511) planes of the fluorite structure of CeO_2 (JCPDS-ICDD Card No. 34–394), respectively. In the case of $Ni(tmhd)_2$ and $Co(acac)_3$ precursor-based NiO_x/CeO_2 (red) and CoO_x/CeO_2 (green) catalysts, no NiO_x and CoO_x peaks were observed, indicating that surface species were finely dispersed on CeO_2 surface. For the $Ni(acac)_2$ precursor based NiO_x/CeO_2 (red) catalysts, however, new peaks were observed at 2.6, 3.0 and 4.7 Å^{-1}, which are attributed to the (111), (200) and (220) planes of NiO (JCPDS-ICDD Card No. 04–0835). In the case of the $Co(acac)_2$ precursor based CoO_x/CeO_2 (green) catalysts, new peaks were

observed at ~2.2, 2.6, 3.1, and 4.4 $Å^{-1}$, which are attributed to the (220), (311), (400) and (511) planes of Co_3O_4 (JCPDS-ICDD Card No. 97–006-9369). This result provided that the dispersion of surface species could be affected by the different types of precursors (e.g., monomeric, dimeric, and trimeric). It should be noted that the peak positions of CeO_2 on the NiO_x/CeO_2 and CoO_x/CeO_2 XRD patterns were not shifted, confirming that the majority of CeO_2 structure was not changed and $Ce_xM_{1-x}O_2$ solid solutions were not formed. Based on the results, it was expected that the deposition of extremely small-sized metal particles distributed over CeO_2 is possible using the monomeric structure-based precursors. This prediction comes as no diffraction peaks were observed for CrO_x/CeO_2, MnO_x/CeO_2, FeO_x/CeO_2, and CuO_x/CeO_2 catalysts' XRD patterns as shown in Fig. S2.

3.3. ICP-OES analysis

To confirm the weight percentage (wt%) of metal loading in the synthesized catalysts, ICP-OES was utilized, and the results are presented in Table 1. The metal loadings for most catalysts closely aligned with the target value (3 wt%). Although it is in an acceptable range, MnO_x ($Mn(tmhd)_3$)/CeO_2, and CuO_x ($Cu(acac)_2$)/CeO_2 catalysts showed a slightly lower weight loading than the target value. In all cases, the metal weight loss during synthesis was lower than that observed in the TGA, due to the adsorption of the precursors by the high-surface-area supports. The results confirm that the precursors do not vaporize out of the system, and it is feasible to use OP-CVD method for synthesizing the supported metal oxide (and possibly further reduced up to metal) catalyst with a desired metal loading.

3.4. SEM-EDX analysis

The SEM images and EDX elemental mapping of the NiO_x/CeO_2 and CoO_x/CeO_2 catalysts are displayed in Fig. 4. For the NiO_x/CeO_2 catalysts prepared using $Ni(tmhd)_2$ and CoO_x/CeO_2 using $Co(acac)_3$, the locations of the metal particles, M (M = Ni or Co), as observed in SEM images, matched well with those of Ce, as shown in Fig. 4a-a'' and 4c-c''. This indicates that the metals are well dispersed across the CeO_2 support. In contrast, the distribution of M (M = Ni or Co) in the NiO_x/CeO_2 prepared using $Ni(acac)_2$ and CoO_x/CeO_2 using $Co(acac)_2$ was found to be heterogeneous, characterized by the presence of chunks (or agglomerations) of M, as depicted in Fig. 4b'' and 4d''. It is noteworthy that the location of M does not align with the location of Ce, suggesting that the chunks (or agglomerations) of M are not situated on the CeO_2 but exist as bulk. This indicates a lack of dispersion in the case of oligomeric precursors. Additionally, the SEM/EDS images for the Cr, Mn, Fe, and Cu-based catalysts (Fig. S3), which utilized monomeric precursors, also demonstrated a well-matched distribution of M and Ce, indicating that the metals were well dispersed on the CeO_2 support.

3.5. CO pulse chemisorption

As shown in Fig. S4, the surface of catalysts was saturated with CO chemisorption and passing 7 pulses of CO were sufficient to serve this purpose. The calculation results obtained from CO pulse chemisorption experiments are presented in Table 2. For NiO_x/CeO_2, a higher metal dispersion (20.4%) was obtained when synthesized by the monomeric $Ni(tmhd)_2$ precursor. The metal dispersion was lowered to 12.2% when

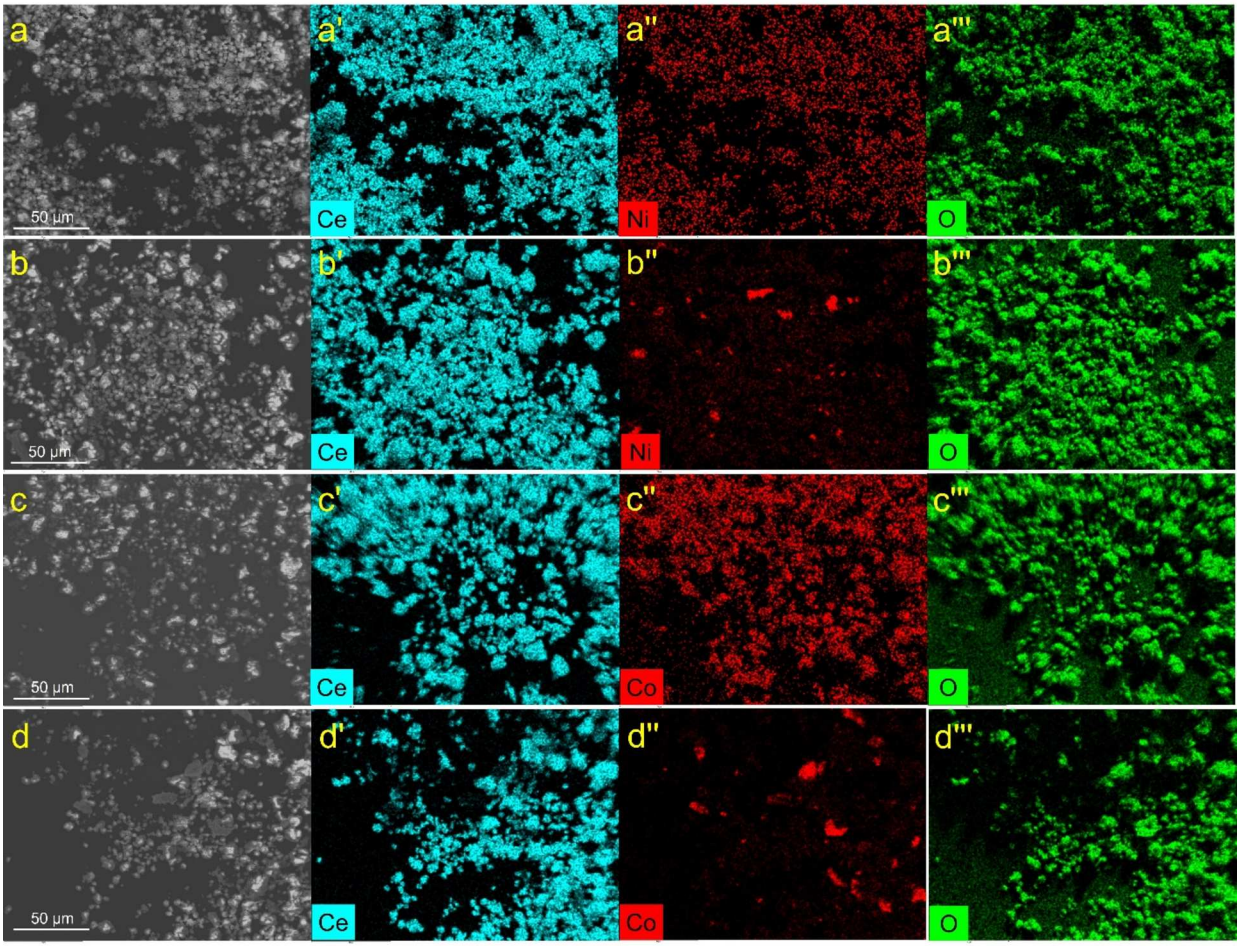

Fig. 4. SEM and EDX mapping for 3% NiO_x/CeO_2 catalyst prepared by (a-a''') $Ni(tmhd)_2$, and (b-b''') $Ni(acac)_2$; and 3% CoO_x/CeO_2 catalysts prepared by (c-c''') Co $(acac)_3$; and (d-d''') $Co(acac)_2$.

Table 2
CO pulse chemisorption of 3% NiO_x/CeO_2 and 3% CoO_x/CeO_2 catalysts.

Samples	Metal dispersion (%)	Average particle diameter (nm)	Adsorbed CO (cm^3 [STP])
NiO_x/CeO_2 (Ni $(tmhd)_2$)	20.4	5.0	0.0579
NiO_x/CeO_2 (Ni $(acac)_2$)	12.2	8.3	0.0348
CoO_x/CeO_2 (Co $(acac)_3$)	25.9	3.9	0.0708
CoO_x/CeO_2 (Co $(acac)_2$)	14.3	7.0	0.0404

NiO_x/CeO_2 is prepared from $Ni(acac)_2$ precursor. Similar trend was observed for CoO_x/CeO_2 catalyst, wherein $Co(acac)_3$ provided higher (25.9%) dispersion of Co than that from $Co(acac)_2$ (14.3%). As a result, the catalysts prepared with monomeric precursors recorded smaller average particle size and higher total CO adsorption on the catalysts' surface (Table 2).

3.6. X-ray absorption spectroscopy

X-ray Absorption Spectroscopy (XAS) analysis was conducted to elucidate the local structure of cobalt in the CoO_x/CeO_2 samples. Fig. 5 displays the XAS data for CoO_x/CeO_2, alongside CoO and Co_3O_4 standards for comparison. The X-ray Absorption Near Edge Structure (XANES) data (Fig. 5a) and extended XAFS (EXAFS) data (Fig. 5b) revealed that the CoO_x/CeO_2 sample prepared from the $Co(acac)_2$ precursor closely resembles Co_3O_4, whereas the sample prepared from $Co(acac)_3$ differ from both CoO and Co_3O_4. We also note that the $Co(acac)_3$ sample is likely a physical mixture of the two phases of Co: the one corresponding to CoO and the other to Co_3O_4, as evident by the presence of several isosbestic points in Fig. 5a. Linear combination analysis of the XANES spectra of CoO_x/CeO_2 samples prepared using two different precursors fitted with Co_3O_4 and CoO standards (Fig. S5) confirms this hypothesis. The LCF analysis obtained the contributions of Co_3O_4 in CoO_x/CeO_2 samples prepared from $Co(acac)_2$ and $Co(acac)_3$ to be 88 and 66 %, respectively.

Despite the analysis of XANES spectra of the both samples points at the relatively simple situation of either predominantly Co_3O_4-like phase for one sample, and a mixture of Co_3O_4 and CoO phases for the other, the XANES region of the absorption coefficient has very low sensitivity to the bonding disorder. Fig. 5b shows the EXAFS data for these samples that contain notable differences. Specifically, the CoO_x/CeO_2 derived from $Co(acac)_2$ showed peaks nearly identical to those of Co_3O_4, whereas the CoO_x/CeO_2 derived from $Co(acac)_3$ displayed significantly lower intensity peaks, suggesting either a reduced coordination number (CN) around the Co atom or enhanced disorder, or both effects. The first part of these findings was consistent with XRD results, where the Co $(acac)_2$-based CoO_x/CeO_2 exhibited peaks characteristic of Co_3O_4, indicating the presence of large chunks of surface species creating

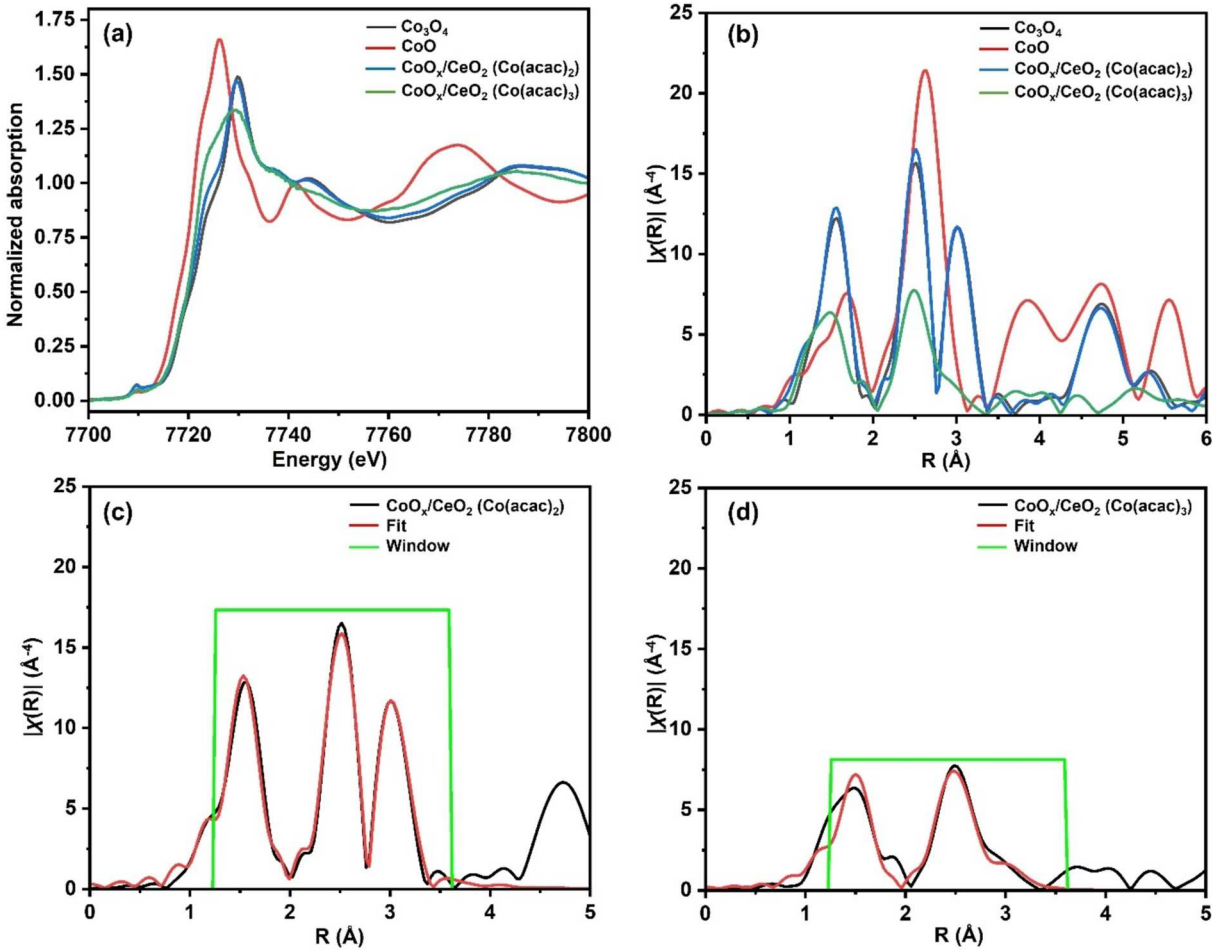

Fig. 5. Comparison of the 3 % CoO_x/CeO_2 prepared by using $Co(acac)_2$ and $Co(acac)_3$ precursors along with Co_3O_4 and CoO as a reference. The data are shown in (a) energy space (XANES region), (b) Fourier transform magnitude of the k^3-weighted EXAFS spectra, (c) EXAFS fitting of 3 % CoO_x/CeO_2 prepared by using $Co(acac)_2$, (d) EXAFS fitting of 3 % CoO_x/CeO_2 prepared by using $Co(acac)_3$. The k-range used for the Fourier transforms was from 2 $Å^{-1}$ to 14 $Å^{-1}$. The *R* range of EXAFS fitting was 1.25–3.6 Å.

inhomogeneity in the catalyst.

EXAFS fitting (Fig. 5c,d) was performed using Co_3O_4 as the model structure, incorporating the Co-O first shell, Co-Co second shell, and Co-Co third shell as derived from theoretical calculations (FEFF). The outcomes of the fitting are presented in Table 3. For the CoO_x/CeO_2 derived from $Co(acac)_2$, the coordination number for the first shell Co-O was determined to be 4.13±0.45, and the CoO_x/CeO_2 derived from $Co(acac)_3$ showed a significantly lower first shell coordination number of 2.61±0.57. The Co-O bond distance was recorded as 1.917±0.004 Å for the $Co(acac)_2$-based CoO_x/CeO_2, which agrees with the crystal structure of Co_3O_4 (COD ID: 1526734) and the EXAFS fitting of the Co_3O_4 (Fig. S6a) reference sample in Table 3. However, the CoO_x/CeO_2 derived from $Co(acac)_3$ exhibited slightly shorter Co-O bond distances of 1.898 ±0.010 Å. This shortening in the Co-O distance can be explained by the presence of square planar Co-O species, which is reported Co-doped nanocrystals of CeO_2 [25], which is also in agreement with the lowering in the coordination number of the first shell Co-O contribution. We also considered the potential influence of a CoO sub-phase; however, as shown in Table 3 and Fig. S6b, the presence of CoO would contribute to elongating the Co-O bond distance. Therefore, we concluded that another species is indeed responsible for the observed shortening of the Co-O bond distance. Additionally, the coordination number for the third shell Co-Co bond was 7.4±1.4 for the $Co(acac)_2$-based sample, compared to a markedly lower 0.36±0.54 for the $Co(acac)_3$-based catalyst, highlighting significant change in the particle size of the surface species or its structural differences induced by the choice of precursor.

Similarly, the NiO_x/CeO_2 samples prepared from the $Ni(acac)_2$ precursor showed XANES (Fig. 6a) features characteristic of NiO, while the sample prepared from $Ni(tmhd)_2$ exhibited distinct features, indicating different local environments. Similar to Co-based catalysts, EXAFS data (Fig. 6b) for NiO_x/CeO_2 derived from $Ni(tmhd)_2$ (monomer) showed very lower intensity peaks than that derived from $Ni(acac)_2$ (not monomer) and bulk NiO, providing evidence for reduced CN for Ni atom and/or relatively large bonding disorder. This data is in agreement with the respective XRD data, confirming homogeneous catalysts from the precursor forming a stable monomer structure. EXAFS fitting was also performed for the NiO_x/CeO_2 (Fig. 6c,d) and the results are presented in Table 4. For NiO_x/CeO_2 derived from $Ni(acac)_2$, the coordination number for the first shell Ni-O was determined to be 4.6±0.8, and the NiO_x/CeO_2 derived from $Ni(tmhd)_2$ showed a higher first shell coordination number of 5.2±1.9, respectively. The coordination number for the Ni-Ni bond in the $Ni(acac)_2$-based sample was 11.0±2.0, while it could not be included in the fit for the $Ni(tmhd)_2$-based sample, suggesting significant structural differences between the two NiO_x/CeO_2 samples.

3.7. RWGS reaction activity data

The prepared catalysts were subjected to the RWGS reaction, and the obtained data is presented in Fig. 7 and Fig. S7. The CO activity for NiO_x/CeO_2 and CoO_x/CeO_2 with increasing temperatures is shown in Fig. 7a. The breakthrough point of RWGS reaction for NiO_x/CeO_2 from $Ni(tmhd)_2$ and $Ni(acac)_2$ were observed to be at ~300 and ~280 °C, respectively (Fig. 7a,b). As observed from Fig. 7c, the progress of RWGS reaction by NiO_x/CeO_2 from $Ni(tmhd)_2$ was dominated up to 400 °C, however, the one from $Ni(acac)_2$ showed better activity towards CO (Fig. 7a). In addition, Fig. 7b also shows that higher CO selectivity was achieved by the NiO_x/CeO_2 prepared by $Ni(acac)_2$. Interestingly, CO selectivity in both Ni catalysts showed a decrease (300 – 350 °C) and then a gradual increase (> 350 °C) trend with temperature. Fig. 7d shows the production of CH_4 for the catalysts. It was observed that the decrease in CO activity was due to the formation of CH_4 (methanation reaction). Overall, the Ni-based catalysts could not achieve complete CO selectivity up to 500 °C.

The RWGS reaction for CoO_x/CeO_2 from $Co(acac)_3$ and $Co(acac)_2$ progresses from ~330 and ~300 °C, respectively (Fig. 7a-c). It was observed from Fig. 7a and c that CoO_x/CeO_2 from $Co(acac)_3$ showed gradual and continuous progress in the RWGS reaction with temperature. Moreover, it was also able to achieve complete (~100%) CO selectivity throughout the experiment. However, Fig. 7b reveals that the CoO_x/CeO_2 catalyst prepared from $Co(acac)_2$ reached complete CO selectivity at 450 °C. To support this, a side methanation step was confirmed (Fig. 7d) from 300 – 450 °C. The overall activity of CoO_x/CeO_2 from $Co(acac)_3$ was superior in terms of activity and selectivity at high temperature.

The RWGS reaction data for the 3% MO_x/CeO_2 (M=Cu, Fe, Mn, Cr) are presented in Fig. S7. All these catalysts showed ~100 % CO selectivity (no methanation reaction). Upto 500 °C, the order of these catalyst in terms of activity are: CuO_x/CeO_2 > FeO_x/CeO_2 > CrO_x/CeO_2 > MnO_x/CeO_2.

4. Discussions

Feasibility and effectiveness of synthesis via OP-CVD

Selection of an appropriate metal precursor for the synthesis of MO_x over the CeO_2 support is the first step. For brevity, the Ni-based precursors are considered here as an example. In section 3.1, two precursors for Ni are presented viz. $Ni(acac)_2$ and $Ni(tmhd)_2$. Herein, OP-CVD is designed with the selection of appropriate precursors that tend to stabilize and preserve its monomeric structure under controlled thermal conditions. From Fig. 2b complete vaporization of $Ni(tmhd)_2$ was observed, indicating that "tmhd" had enough steric hindrance to

Table 3
EXAFS Fitting results of the 3% CoO_x/CeO_2 prepared by using $Co(acac)_2$ and $Co(acac)_3$.

Sample	CN(Co-O)	R (Å)	σ^2 ($Å^2$)	N(Co-Co) Second shell	R (Å)	σ^2 ($Å^2$)	N(Co-Co) Third shell	R (Å)	σ^2 ($Å^2$)	ΔE (eV)
CoO_x/CeO_2 prepared by $Co(acac)_2$	4.13± 0.45	1.917± 0.004	0.0017± 0.0006	3.53± 0.56	2.856± 0.004	0.0026± 0.0008	7.37± 1.44	3.361± 0.005	0.0060± 0.0012	0.4± 0.7
CoO_x/CeO_2 prepared by $Co(acac)_3$	2.61± 0.57	1.898± 0.010	0.0026± 0.0013	2.04± 0.55	2.835± 0.001	0.0032± 0.0014	0.36± 0.54	3.408± 0.024	0 ± 0.006	−1.7± 2.3
Co_3O_4[a]	4.67± 0.62	1.915± 0.005	0.0030± 0.0009	4.86± 0.99	2.860± 0.006	0.0048± 0.0011	7.68± 1.82	3.365± 0.007	0.0060± 0.0014	1.2± 0.9
Co_3O_4[b]	5.33	1.916± 0.006	0.0038± 0.0007	4	2.858± 0.005	0.0038± 0.0005	8	3.363± 0.006	0.0063± 0.0006	1.1± 0.9
CoO[c]	6.52± 1.22	2.113± 0.009	0.0078± 0.0019	14.5± 1.4	3.011± 0.005	0.0081± 0.0007				−1.6± 0.9

[a] Co_3O_4 was fitted with the same model and parameters used to fit the 3% CoO_x/CeO_2 prepared by using $Co(acac)_2$.
[b] Co_3O_4 fitted with coordination numbers fixed to the Co_3O_4 crystal structure to obtain the amplitude reduction factor ($S_0^2 = 0.79$).
[c] The *R* range of EXAFS fitting was 1.25–3.0 Å.

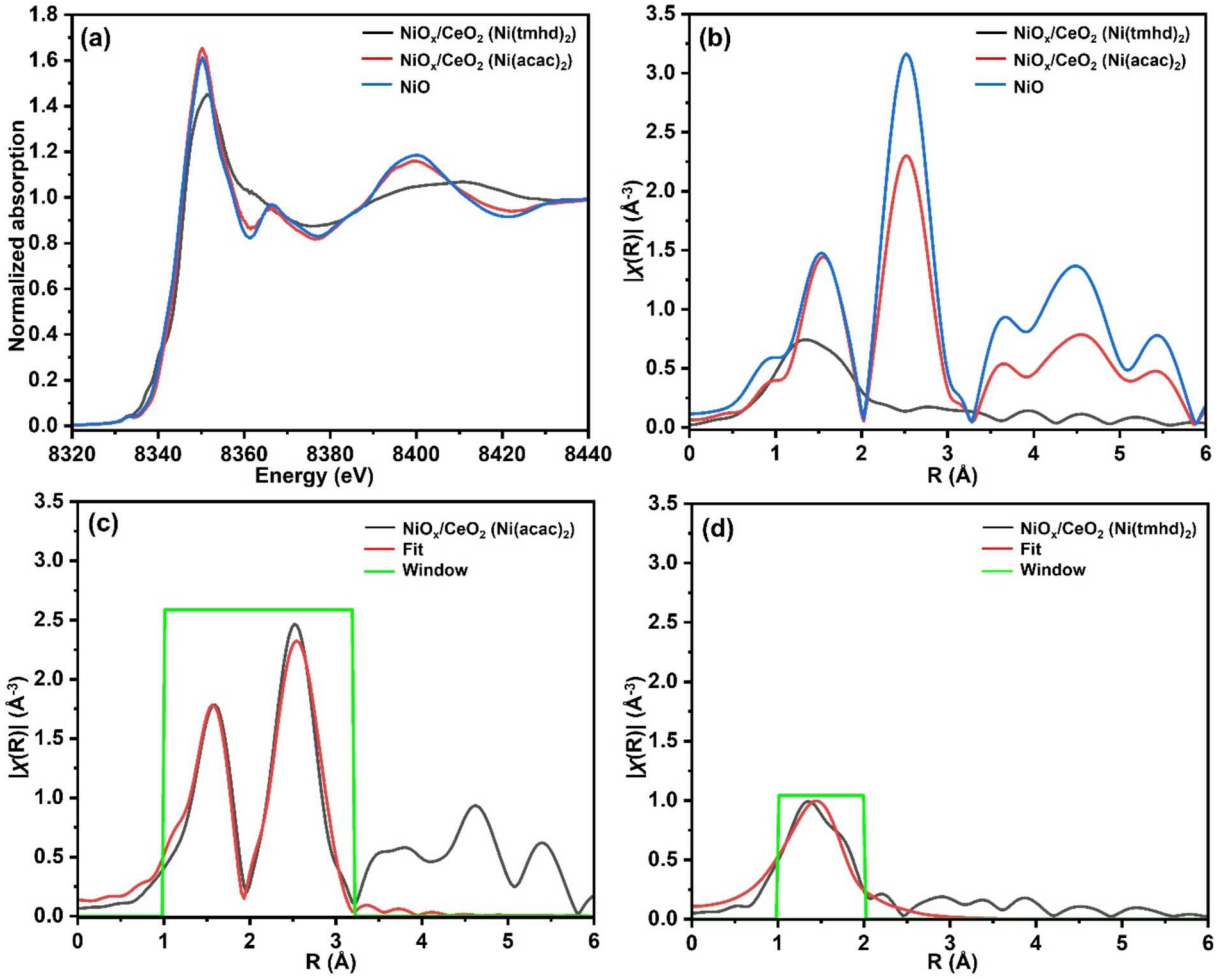

Fig. 6. Comparison of the 3 % NiO_x/CeO_2 prepared by using $Ni(acac)_2$ and $Ni(tmhd)_2$ precursors along with NiO as a reference. The data are shown in (a) energy space (XANES region), (b) Fourier transform magnitude of the k^2-weighted EXAFS spectra, (c) EXAFS fitting of 3 % NiO_x/CeO_2 prepared by using $Ni(acac)_2$, (d) EXAFS fitting of 3 % NiO_x/CeO_2 prepared by using $Ni(tmhd)_2$. The k-range used for the Fourier transforms was from 2 $Å^{-1}$ to 11 $Å^{-1}$. The *R* range of EXAFS fitting was 1.0–3.2 Å for 3 % NiO_x/CeO_2 prepared by using $Ni(acac)_2$ and 1.0–2.0 Å for 3 % NiO_x/CeO_2 prepared by using $Ni(tmhd)_2$, respectively.

Table 4
EXAFS Fitting results of the 3% NiO_x/CeO_2 prepared by using $Ni(acac)_2$ and $Ni(tmhd)_2$.

Fit	S_0^2	N(Ni-O)	R (Å)	σ^2 ($Å^2$)	N(Ni-Ni)	R (Å)	σ^2 ($Å^2$)	ΔE (eV)
NiO_x/CeO_2 prepared by$Ni(acac)_2$	1.00	4.6± 0.8	2.06± 0.01	0.005± 0.002	11.0± 2.0	2.965± 0.009	0.009± 0.002	1.9± 4.3
NiO_x/CeO_2 prepared by$Ni(tmhd)_2$	1.00	5.2± 1.9	2.00± 0.04	0.018± 0.008	a	–	–	−3.3± 3.6

a: Ni-Ni shell in 3% NiO_x/CeO_2 prepared from $Ni(tmhd)_2$ could not be included in the fit.

stabilize the monomeric structure as we expected. This satisfies the first criterion for the selection of precursors (section 1.2) for a stable monomeric structure. As evident from Fig. 2a, "acac" group could not stabilize the monomeric structure of $Ni(acac)_2$ and formed a trimer in the solid state (Fig. 3) resulting in high molecular weight and low vapor pressure, favoring the decomposition of the complex over vaporization. It is clearly observed from Fig. 2b that the $Ni(tmhd)_2$ precursor was completely vaporized < 250 °C, providing sufficient vapor pressure, and this satisfies the second criterion of the design. Again, as the decomposition of the complex is favored with the "acac" group, thus it could not be considered for the vapor formation. Both the compounds could satisfy the third criterion (C, H, and O elements) to reduce the possibility of introducing the heteroatom to the system, which might lead to catalyst poison. Lastly, TGA analysis of $Ni(acac)_2$ (Fig. 2a) and Ni $(tmhd)_2$ (Fig. 2b) shows decomposition and vaporization, respectively, confirming the suitability of the latter as a precursor to making Ni-based supported catalysts via the OP-CVD method. After confirming this selection process, further vapor control steps (Fig. 2c,f) are being carried out to determine the synthesis conditions.

After the precursor selection and determining the synthesis conditions protocol, a series of 3% MO_x/CeO_2 (M = Ni, Co, Fe, Mn, Cr, Cu) catalysts were prepared. Each batch of catalyst requires ~8h for the complete preparation, which is shorter than that required by other synthesis methods. The Ni-based catalysts from $Ni(acac)_2$ and $Ni(tmhd)_2$

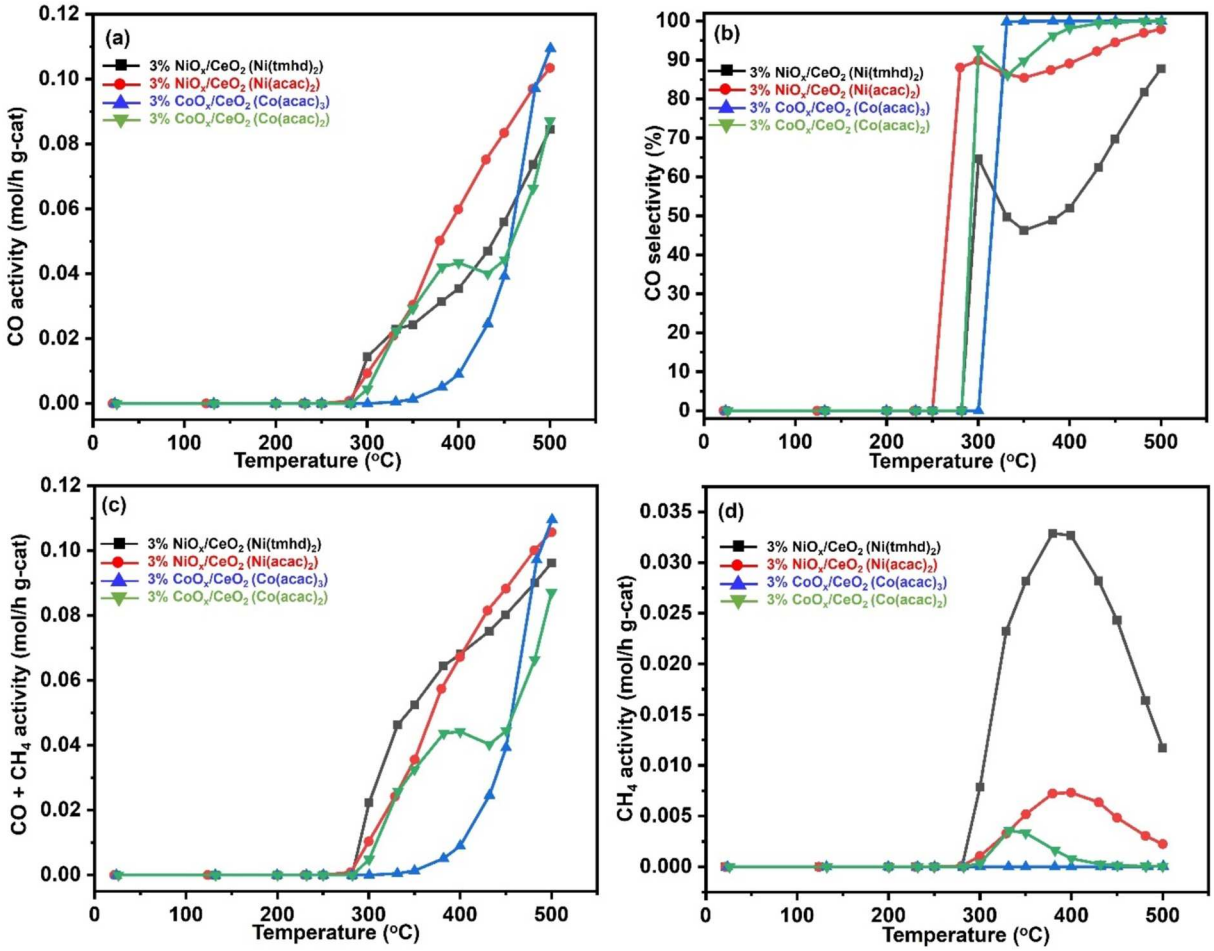

Fig. 7. RWGS reaction activity data: (a) CO activity; (b) CO selectivity; (c) CO + CH_4 activity; and (d) CH_4 activity of NiO_x/CeO_2 and CoO_x/CeO_2 catalysts with temperature.

were tested for XRD. Fig. 3 shows that NiO peaks were present with the catalyst prepared by $Ni(acac)_2$, whereas these were absent with that obtained from $Ni(tmhd)_2$. This data provides the first glimpse of the effective dispersion and fine particle size of NiO from the monomeric $Ni(tmhd)_2$. This was further confirmed by EDX mapping (Fig. 4a"), whereas the large chunk sizes of Ni were seen from EDX mapping (Fig. 4b") for NiO_x/CeO_2 ($Ni(acac)_2$). To prove a triple check on effective metal dispersion (Ni and Co), CO pulse chemisorption results (Table 2) showed a higher degree of metal dispersion when catalysts were synthesized via OP-CVD method using monomeric precursors. The smaller particle size developed using monomeric precursor facilitated this thorough dispersion of metal species (MO_x) over the ceria support. The

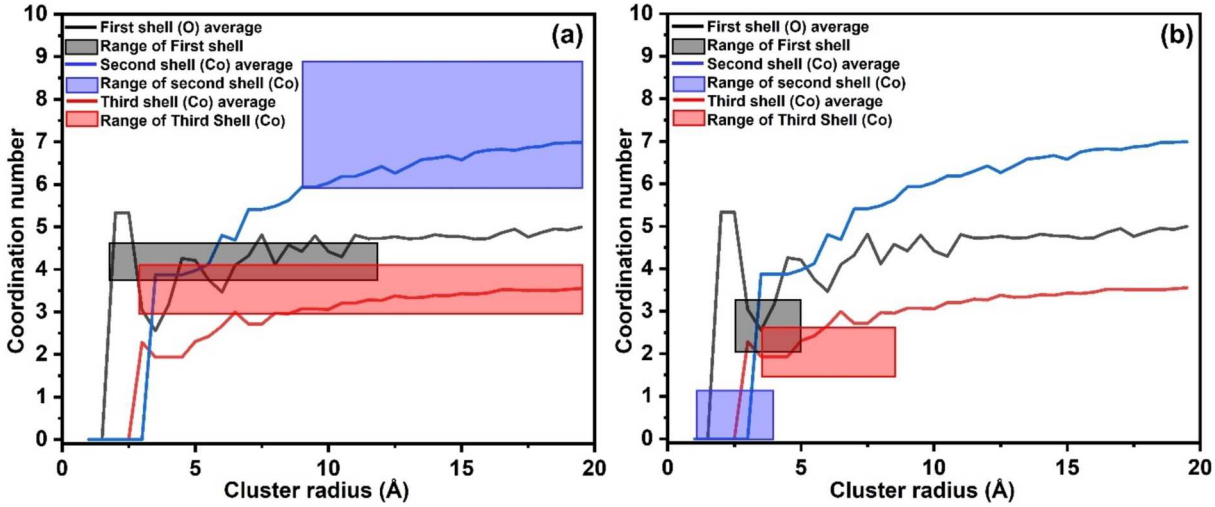

Fig. 8. Relationship of coordination number (CN) versus cluster size of Co_3O_4. The square box represents the possible range of CN obtained from EXAFS analysis of CoO_x/CeO_2 prepared from (a) $Co(acac)_2$; and (b) $Co(acac)_3$ precursor.

effective target loading was studied from ICP-OES analysis which is a bulk technique. As per the hypothesis, there is no vaporization in Ni $(acac)_2$. Therefore, a complete target load value (3% Ni) should be matched as there is no metal loss. Table 1 shows that NiO_x/CeO_2 (Ni $(acac)_2$) has an exact 3% Ni loading. It is also evident that Ni weight loading in NiO_x/CeO_2 $(Ni(tmhd)_2)$ closely matched (2.98%) to the target value confirming that the decided dispersion temperature at incipience of vaporization was effective in successful adsorption on CeO_2 with negligible precursor loss out of the reactor system. Similar results were also observed for CoO_x/CeO_2 ($Co(acac)_3$ and $Co(acac)_2$) and other MO_x/CeO_2 catalysts. While XRD provides information about the periodic structure and relatively large particle sizes, EXAFS is used to analyze the structural information of well-dispersed samples. Fig. 8 plots the relationship between the coordination number of quasi-spherical clusters derived from the Co_3O_4 crystal structure with varying cluster radii. The coordination number varied by changing the center of the cluster from the octahedral site to the tetrahedral sites of the Co and only the average coordination number is shown in Fig. 8 for clarity. Following the methodology developed in [26–28], by overlaying the coordination numbers obtained from EXAFS, including error bars, we estimated the possible cluster radius ranges for the catalysts: 9.0 to 12.0 Å for those made from the $Co(acac)_2$ precursor, and 2.7 to 3.1 Å for those made from the $Co(acac)_3$ precursor. It's important to note that these cluster radius estimates with an assumption of identical, quasi-spherical clusters. However, both samples made from the $Co(acac)_2$ and $Co(acac)_3$ precursor are heterogeneous (contain two phases), and the catalyst made from the $Co(acac)_3$ precursor includes contributions from square planar structures. Due to the several approximations described above, our analysis provides a qualitative understanding of the particle sizes, giving their lower bounds. We also attempted a similar analysis for NiO, but it was unsuccessful due to the lack of third shell information, which is necessary to narrow down the possible coordination number range.

In both the Co and Ni cases, using oligomeric precursors tends to result in large particle chunks with heterogeneous distribution. This reflects the initial heterogeneous mixture of the precursor and CeO_2. In contrast, using monomeric precursors allows for better dispersion over CeO_2 through the vapor phase during synthesis. In many cases, high dispersion or small particle sizes are key to higher catalytic activity since the percentage of the metals exposed to the surface increases as the nanoparticles become smaller. Additionally, this can dramatically increase or change selectivity by limiting the possible catalytic sites that substrates can access. One example is the Reverse Water Gas Shift (RWGS) reaction, where dispersed and small particles of Ni give CO selectivity, while larger particles lead to CH_4 selectivity.

Effect of catalyst design via OP-CVD on RWGS reaction activity

The ever-increasing CO_2 levels in the atmosphere have been a matter of serious concern, and thus converting it to useful commercial chemicals could be of interest. Reverse water–gas shift (RWGS) reaction [14,15] can solve this issue according to the following reaction: $CO_2 + H_2 \rightarrow CO + H_2O\ \Delta H_r = 41.3 kJ/mol$. The obtained products can then be further utilized to produce various useful chemicals such as methanol, olefins, gasoline, etc. The thermodynamic stability of CO_2 is a major challenge in converting it to more useful products via the RWGS reaction [29–31]. As a result, these reactions often require high temperatures. Thus, activation of CO_2 by catalytic means turns out to be extremely important. Transition metal complexes have shown the ability to activate the C=O bond of CO_2 [32]. First-row transition metals (3d) have become a great focus of interest. Lu et al. studied Fe(I)-mediated reductive cleavage and coupling of CO_2 [33]. The authors reported that reductive cleavage of CO_2 was possible via the O-atom transfer. Isaacs et al. reported the electrocatalytic reduction of CO_2 using Co, Ni, and Fe [34]. The authors claimed that the chemical nature of the metal center plays an important role in the reduction of CO_2. The authors also mentioned that reduced metal centers were not sufficient for the C=O breaking.

The MO_x/CeO_2 catalysts prepared by the OP-CVD method showed interesting results for the RWGS reaction (Fig. 7 and S7). The size and composition of the active site are dependent on the appropriate precursor selection, and its effect on RWGS activity was also observed (Fig. 7). Different transition metals gave varied RWGS reaction progress in terms of CO activity and selectivity (Fig. S7). Interestingly, all MO_x/CeO_2 synthesized using a monomeric precursor provided complete CO selectivity, with NiO_x/CeO_2 as an exception. In this study, the selection of effective precursors to produce quality catalysts has been explained and proved in the sections so far. The CoO_x/CeO_2 catalyst from monomeric $Co(acac)_3$ showed uniformly dispersed and smaller particle size of ~0.6 nm with lower coordination numbers, as a result, higher activity and complete selectivity towards CO were possible. However, lower selectivity were observed with CoO_x/CeO_2 from non-monomeric Co $(acac)_2$. This corroborates that the synthesis design plays a crucial role in the performance of the catalysts. Similarly, the Cu, Fe, Mn, and Cr-based catalysts prepared from the monomeric precursors showed ~100% CO selectivity, almost eliminating the methanation step. However, the progress of the reaction was observed to be highly metal-selective and the highest activity (~0.11 mol/h g-cat) was shown by CuO_x/CeO_2 catalyst. This activity data is either superior or comparable with the previously reported data (Table 5). The authors would also like to bring to notice that the characterization results of Ni-based catalysts from monomeric precursor showed effective dispersion and target loading, but could not achieve the desired CO selectivities (Fig. 7b). In a study conducted by L. Lin et al., NiO_x/CeO_2 catalysts were reported to have strong correlation with the particle size of the Ni nanoparticles and the CO selectivity of RWGS reaction, where small particle size will result to CO selective reaction (~2 nm) and large particle size (> 2nm) will result to methanation [35]. Lin et al. also observed that the metal loading of 3 wt% Ni was in the range where the particle size was large enough to show high methanation selectivity, and the concentration of <0.5 wt% was in the range where the particle size was small enough to show high CO selectivity [35]. In this study, negligible $Ni(acac)_2$ should be able to vaporize since its decomposition is favored, to get a heterogeneous distribution of Ni as NiO_x on ceria. However, $Ni(tmhd)_2$ will lead to uniform distribution of Ni as NiO_x on ceria. The difference in the CO selectivity can be explained by the particle size of the active sites, which is strongly correlated with the effective metal loading. To confirm this, RWGS reaction actvity was tested over 0.1, 0.5 and 3 wt%Ni in NiO_x/CeO_2 catalysts (Fig. S8) prepared by $Ni(tmhd)_2$ precursor, and the improved selectivity for CO with decreasing Ni loading was observed. In a study by Y. Qi et al., higher adsorption energy of CO with Ni species was reported that led to strong binding of CO that can further hydrogenate it to form methane at lower temperatures [41]. It is evident from the Ni loading on RWGS reaction actvity that more surface coverage (higher cluster size) of Ni will have higher affinity to strongly bind produced CO, generating higher amounts of methane and lowering the desired CO selectivity. Therefore, lower Ni loading (e.g., 0.1%) could desorb the produced CO easily than that by higher Ni loading (e.g., 3%)

Table 5
RWGS reaction activity comparison table.

Sr. No.	Catalyst	Temperature (°C)	H_2: CO_2	Activity (mol/h g-cat)	Reference
1.	15 % Cu/CeO_2	500	4	1.87	[32]
2.	28.1 % Ni/CeO_2	300	4	0.0016	[35]
3.	CuO_x/CeO_2	400	1	0.046	[36]
4.	Pt/CeO_2	375	1	0.58×10^{-9}	[37]
5.	1 % Cu/β-Mo_2C	600	2	1.36	[38]
6.	K_{80}-Pt/L	500	1	0.16	[39]
7.	Cu/CeO2-hs	500	3	1.2	[40]
8.	3 % CuO_x/CeO_2	500	1	0.11	This study

in NiO_x/CeO_2 and thus recorded higher CO selectivity than the latter. Although the selectivity of the reaction was not optimized for the RWGS reaction, we can clearly state that our design of the precursor leads to efficient and uniform dispersion of the metal precursors, as shown in the catalyst characterization and as well as in terms of the reactivity. For the actual application, one should consider if they want a dispersed catalyst or not, along with optimizing the combination of the metal and the support, since most of the activity and selectivity of the reaction (including RWGS) are extensively dependent on the characteristics of the active sites of the catalyst. Our method can control by the design protocol of OP-CVD method and the type of metal to be used to serve the purpose.

5. Conclusions

The OP-CVD process was proposed based on specific criteria for precursor selection: (i) stable monomeric structure; (ii) vapor pressure to check suitability; (iii) ligand composition (C, H, O); and (iv) thermal stability to ensure clean vaporization. The deposition and rapid fixation processes were crucial for effective gas–solid interaction and fixing the achieved location of the metal sites, respectively. Through this approach to precursor design and catalyst synthesis, a method capable of producing highly dispersed small-sized active site heterogeneous catalyst was proposed. The SEM-EDX, ICP-OES, XRD, CO pulse chemisorption, and XAS analysis were used to confirm the critical role of monomeric precursors in metal dispersion. Cluster size analysis via coordination numbers obtained from EXAFS further demonstrated that the use of monomeric precursors leads to the formation of small MO_x particles. Therefore, small, finely dispersed MO_x active species on ceria supports were successfully developed using the proposed OP-CVD method. The RWGS reaction data showed that the CO activity and selectivity were dependent on metal, metal-precursor, and particle size. Higher CO activity of > 0.1 mol/h g-cat was observed for Cu and Co-based catalysts. The CO selectivity of ~100% was achieved by all the MO_x/CeO_2 catalysts, except for the Ni, prepared via the OP-CVD method using precursors stabilized as monomers. In OP-CVD, the design of the precursor is independent of the specific metal, allowing it to be applied to a wide range of other metals or elements. We are further working on extending this approach to 4d and 5d metals, varied support materials with inert (e.g., Al_2O_3 and SiO_2), different MSI-redox ability (e.g., CeO_2-ZrO_2, TiO_2) and high surface area (e.g., activated carbon) properties, as well as exploring the application of OP-CVD for other catalytic reactions.

CRediT authorship contribution statement

Amol Pophali: Writing – review & editing, Writing – original draft, Visualization, Validation, Methodology, Investigation, Formal analysis, Data curation, Conceptualization. **Ryuichi Shimogawa:** Writing – review & editing, Writing – original draft, Methodology, Investigation, Formal analysis, Data curation, Conceptualization. **Lihua Zhang:** Resources, Investigation. **Gihan Kwon:** Resources, Investigation, Data curation. **Kwangsuk Yoon:** Investigation, Formal analysis. **Jangeon Roh:** Formal analysis, Investigation. **Do Heui Kim:** Resources, Supervision. **Hocheol Song:** Supervision, Resources. **Anatoly I. Frenkel:** Writing – review & editing, Resources, Funding acquisition. **Taejin Kim:** Writing – review & editing, Writing – original draft, Supervision, Resources, Project administration, Investigation, Funding acquisition, Conceptualization.

Declaration of competing interest

The authors declare that they have no known competing financial interests or personal relationships that could have appeared to influence the work reported in this paper.

Acknowledgement

TJK acknowledges funding support from the National Science Foundation (NSF-CBET-2050824). AIF acknowledges the support from National Science Foundation (NSF CHE 2102299). This research used the beamlines 7-BM and 28-ID-1 of the National Synchrotron Light Source II (NSLS-II) and the Materials Synthesis and Characterization Facility of Center for Functional Nanomaterials (CFN), which are U.S. Department of Energy (DOE) Office of Science User Facilities at Brookhaven National Laboratory under Contract No. DE-SC0012704. 7-BM beamline operations were supported in part by the Synchrotron Catalysis Consortium (US DOE, Office of Basic Energy Sciences, Grant No. DE-SC0012335). The authors thank Drs. P. K. Routh, H. Wang, N. Marinkovic, L. Ma, S. Ehrlich, and A. Tayal for the help on the beamline measurements at 7-BM. DHK acknowledges support from the Carbon Neutral Industrial Strategic Technology Development Program funded by the Ministry of Trade, Industry & Energy (MOTIE) of the Republic of Korea (RS-2023–00261088).

Appendix A. Supplementary data

Supplementary data to this article can be found online at https://doi.org/10.1016/j.cej.2024.158726.

Data availability

Data will be made available on request.

References

[1] S. Bernal, J.J. Calvino, M.A. Cauqui, J.M. Gatica, C. Larese, J.A. Pérez Omil, J. M. Pintado, Some recent results on metal/support interaction effects in NM/CeO2 (NM: noble metals) catalysts, Catal. Today 50 (1999) 175–206.
[2] P.V. Snytnikov, V.A. Sobyanin, V.D. Belyaev, P.G. Tsyrulnikov, N.B. Shitova, D. A. Shlyapin, Selective oxidation of carbon monoxide in excess hydrogen over Pt-, Ru- and Pd-supported catalysts, Appl. Catal. a: General 239 (2003) 149–156.
[3] U. Iriarte-Velasco, J.L. Ayastuy, Z. Boukha, R. Bravo, M.Á. Gutierrez-Ortiz, Transition metals supported on bone-derived hydroxypatite as potential catalysts for the water-gas shift reaction, Renew. Energy 115 (2018) 641–648.
[4] P. Mani, R. Srivastava, P. Strasser, J. Power Sources 196 (2011) 666–673.
[5] A.R. Ardiyanti, S.A. Khromova, R.H. Venderbosch, V.A. Yakovlev, I.V. Melián-Cabrera, H.J. Heeres, Catalytic hydrotreatment of fast pyrolysis oil using bimetallic Ni-Cu catalysts on various supports, Appl. Catal. a: General 449 (2012) 121–130.
[6] J.H. Kwak, L. Kovarik, J. Szanyi, CO_2 Reduction on Supported Ru/Al_2O_3 Catalysts: Cluster Size Dependence of Product Selectivity, ACS Catal. 3 (2013) 2449.
[7] S. Zhang, Y. Li, J. Huang, J. Lee, D.H. Kim, A.I. Frenkel, T. Kim, Effects of Molecular and Electronic Structures in CoO_x/CeO_2 Catalysts on NO Reduction by CO, J. Phys. Chem. C 123 (2019) 7166–7177.
[8] A. Gurbani, J.L. Ayastuy, M.P. González-Marcos, J.E. Herrero, J.M. Guil, M. A. Gutiérrez-Ortiz, Comparative study of CuO–CeO_2 catalysts prepared by wet impregnation and deposition–precipitation, Int. J. Hydrogen Energy 34 (2009) 547–553.
[9] D. Yao, H. Yang, H. Chen, P.T. Williams, Co-precipitation, impregnation and so-gel preparation of Ni catalysts for pyrolysis-catalytic steam reforming of waste plastics, Appl. Catal. b: Environmental 239 (2018) 565–577.
[10] P. Munnik, P.E. de Jongh, K.P. de Jong, Recent Developments in the Synthesis of Supported Catalysts, Chem. Rev. 115 (2015) 6687–6718.
[11] J. Lu, J.W. Elam, P.C. Stair, Synthesis and Stabilization of Supported Metal Catalysts by Atomic Layer Deposition, Acc. Chem. Res. 46 (2013) 1806–1815.
[12] R.J. Gorte, Ceria in catalysis: From automotive applications to the water–gas shift reaction, AIChE J 56 (2010) 1126–1135.
[13] L.P. Teh, H.D. Setiabudi, S.N. Timmiati, M.A.A. Aziz, N.H.R. Annuar, N.N. Ruslan, Recent progress in ceria-based catalysts for the dry reforming of methane: A review, Chem. Eng. Sci. 242 (2021) 116606.
[14] S.-Y. Huang, C.-M. Chang, C.-T. Yeh, Promotion of platinum–ruthenium catalyst for electro-oxidation of methanol by ceria, J. Catal. 241 (2006) 400–406.
[15] S. Karthika, T.K. Radhakrishnan, P. Kalaichelvi, A Review of Classical and Nonclassical Nucleation Theories, Cryst. Growth Des. 16 (2016) 6663–6681.
[16] R.K. Sodhi, S. Paul, An overview or Metal Acetylacetonates: Developing Areas/Routes to New Materials and Applications in Organic Syntheses, Catal. Surv. Asia 22 (2018) 31–62.
[17] P.A. Stabnikov, G.I. Zharkova, I.A. Baidina, S.V. Tkachev, V.V. Krisyuk, I. K. Igumenov, Synthesis and properties of a new ketoiminate derivative of the 2,2,6,6-tetramethylheptane-3,5-dionate ligand to prepare volatile CVD precursors, Polyhedron 26 (2007) 4445–4450.
[18] B. Ravel, M. Newville, ATHENA, ARTEMIS, HEPHAESTUS: data analysis for X-ray absorption spectroscopy using IFEFFIT, J. Synchrotron Radiat. 12 (2005) 537–541.

[19] I. Kotousova, S. Polyakov, Electron-diffraction study of Co_3O_4, Kristallografiya 17 (1972) 661.
[20] B.S. Clausen, G. Steffensen, B. Fabius, J. Villadsen, R. Feidenhans'l, H. Topsøe, In situ cell for combined XRD and on-line catalysis tests: Studies of Cu-based water gas shift and methanol catalysts, J. Catal. 132 (1991) 524–535.
[21] G.J. Bullen, R. Mason, P. Pauling, The Crystal and Molecular Structure of Bis (acetylacetonato)nickel (II), Inorg. Chem. 4 (1965) 456–462.
[22] V.D. Vreshch, J.-H. Yang, H. Zhang, A.S. Filatov, E.V. Dikarev, Monomeric Square-Planar Cobalt(II) Acetylacetonate: Mystery or Mistake? Inorg. Chem. 49 (2010) 8430–8434.
[23] F.A. Cotton, J.J. Wise, The Crystal and Molecular Structure of Bis (2,2,6,6-tetramethylheptane-3,5-dionato) nickel (II), Inorg. Chem. 5 (1966) 1200–1207.
[24] L.S.V. Chrzanowski, M. Lutz, A.L. Spek, α-Tris(2,4-pentanedionato-κ2O,O')cobalt (III) at 240, 210, 180, 150 and 110 K, Acta Crystallogr. C 63 (2007) 283–288.
[25] T.S. Wu, Y.W. Chen, S.C. Weng, C.N. Lin, C.H. Lai, Y.J. Huang, H.T. Jeng, S. L. Chang, Y.L. Soo, Dramatic band gap reduction incurred by dopant coordination rearrangement in Co-doped nanocrystals of CeO_2, Sci. Rep. 7 (2017) 4715.
[26] A.I. Frenkel, C.W. Hills, R.G. Nuzzo, A View from the Inside: Complexity in the Atomic Scale Ordering of Supported Metal Nanoparticles, J. Phys. Chem. B 105 (2001) 12689–12703.
[27] A.I. Frenkel, Solving the structure of nanoparticles by multiple-scattering EXAFS analysis, J. Synchrotron Rad. 6 (1999) 293–295.
[28] D. Glasner, A.I. Frenkel, Geometrical Characteristics of Regular Polyhedra: Application to EXAFS Studies of Nanoclusters, AIP Conference Proceedings 882 (2007) 746–748.
[29] M. González-Castaño, B. Dorneanu, H. Arellano-García, The reverse water gas shift reaction: a process systems engineering perspective, React, Chem. Eng. 6 (2021) 954–976.
[30] L. Wang, W. Chen, D. Zhang, Y. Du, R. Amal, S. Qiao, J. Wu, Z. Yin, Surface strategies for catalytic CO_2 reduction: from two-dimensional materials to nanoclusters to single atoms, Chem. Soc. Rev. 48 (2019) 5310–5349.
[31] L.F. Bobadilla, J.L. Santos, S. Ivanova, J.A. Odriozola, A. Urakawa, Unravelling the Role of Oxygen Vacancies in the Mechanism of the Reverse Water–Gas Shift Reaction by Operando DRIFTS and Ultraviolet–Visible Spectroscopy, ACS Catal. 8 (2018) 7455–7467.
[32] H.-X. Liu, S.-Q. Li, W.-W. Wang, W.-Z. Yu, W.-J. Zhang, C. Ma, C.-J. Jia, Partially sintered copper–ceria as excellent catalyst for the high-temperature reverse water gas shift reaction, Nat. Commun. 13 (2022) 867.
[33] C.C. Lu, C.T. Saouma, M.W. Day, J.C. Peters, Fe(I)-Mediated Reductive Cleavage and Coupling of CO_2: An $Fe^{II}(\mu\text{-}O,\mu\text{-}CO)Fe^{II}$ Core, J. Am. Chem. Soc. 129 (2007) 4–5.
[34] M. Isaacs, F. Armijo, G. Ramírez, E. Trollund, S.R. Biaggio, J. Costamagna, M. J. Aguirre, Electrochemical reduction of CO_2 mediated by poly-M-aminophthalocyanines (M = Co, Ni, Fe): poly-Co-tetraaminophthalocyanine, a selective catalyst, J. Molecular Catalysis a: Chemical 229 (2005) 249–257.
[35] L. Lin, C.A. Gerlac, C. Liu, J. Llorca, S. Yao, N. Rui, F. Zhang, Z. Liu, S. Zhang, K. Deng, C.B. Murray, J.A. Rodriguez, S.D. Senanayake, Effect of Ni particle size on the production of renewable methane from CO_2 over Ni/CeO_2 catalyst, J. Energy Chem. 61 (2021) 602–611.
[36] M. Ronda-Lloret, S. Rico-Francés, A. Sepúlveda-Escribano, E.V. Ramos-Fernandez, CuO_x/CeO_2 catalyst derived from metal organic framework for reverse water-gas shift reaction, Appl. Catal. a: General 562 (2018) 28–36.
[37] A. Sápi, T. Rajkumar, M. Ábel, A. Efremova, A. Grósz, A. Gyuris, K.B. Ábrahámné, I. Szenti, J. Kiss, T. Varga, Á. Kukovecz, Z. Kónya, Noble-metal-free and Pt nanoparticles-loaded, mesoporous oxides as efficient catalysts for CO_2 hydrogenation and dry reforming with methane, J. CO_2 Util. 32 (2019) 106–118.
[38] X. Zhang, X. Zhu, L. Lin, S. Yao, M. Zhang, X. Liu, X. Wang, Y.-W. Li, C. Shi, D. Ma, Highly Dispersed Copper over β-Mo_2C as an Efficient and Stable Catalyst for the Reverse Water Gas Shift (RWGS) Reaction, ACS Catal. 7 (2017) 912–918.
[39] X. Yang, X. Su, X. Chen, H. Duan, B. Liang, Q. Liu, X. Liu, Y. Ren, Y. Huang, T. Zhang, Promotion effects of potassium on the activity and selectivity of Pt/zeolite catalysts for reverse water gas shift reaction, Appl. Catal. B 216 (2017) 95–105.
[40] Y. Zhang, L. Liang, Z. Chen, J. Wen, W. Zhong, S. Zou, M. Fu, L. Chen, D. Ye, Highly efficient Cu/CeO_2-hollow nanospheres catalyst for the reverse water gas shift reaction: Investigation on the role of oxygen vacancies through in situ UV-Raman and DRIFTS, Appl. Surf. Sci. 516 (2020) 146035.
[41] Y. Qi, Y.-A. Zhu, D. Chen, Mechanism investigation and catalyst screening of high-temperature reverse water gas shift reaction, Green, Chem. Eng. 1 (2020) 131–139.